Unraveling Trajectories of Diffusive Particles on Networks

Yunhao Sun*,[1] Zexi Yu*,[1] Christopher J. Obara,[2] Keshav Mittal,[1] Jennifer Lippincott-Schwarz,[2] and Elena F. Koslover[1,*]

[1] *Department of Physics, University of California, San Diego, San Diego, California 92093*
[2] *Janelia Research Campus, Howard Hughes Medical Institute, Ashburn, Virginia 20147*

(Dated: April 6, 2022)

The analysis of single particle trajectories plays an important role in elucidating dynamics within complex environments such as those found in living cells. However, the characterization of intracellular particle motion is often confounded by confinement of the particles within non-trivial subcellular geometries. Here, we focus specifically on the case of particles undergoing Brownian motion within a network of narrow tubules, as found in some cellular organelles. A computational unraveling algorithm is developed to uncouple particle motion from the confining network structure, allowing for an accurate extraction of the underlying one-dimensional diffusion coefficient, as well as differentiating between Brownian and fractional Langevin motion. We validate the algorithm with simulated trajectories and then highlight its application to an example system: analyzing the motion of membrane proteins confined in the tubules of the peripheral endoplasmic reticulum in mammalian cells. We show that these proteins undergo diffusive motion and provide a quantitative estimate of their diffusion coefficient. Our algorithm provides a generally applicable approach for disentangling geometric morphology and particle dynamics in networked architectures.

I. INTRODUCTION

Particle tracking experiments have a long history in the field of soft matter physics, where they are used to analyze the material properties of complex fluids and the dynamic behavior of active media (reviewed in [1, 2]). In recent years, tracking of particles inside living cells has been extensively employed to elucidate the dynamics of cellular components ranging from single molecules [3–5] to vesicular organelles [6–9]. Quantification of *in vivo* particle trajectories can be used to identify state transitions and organelle interactions [9–11], to explore the rheology of intracellular fluids[7, 12], and to establish the underlying physical forces that drive particle motion [6, 13, 14].

A classic analysis approach computes the mean square displacement (MSD) of particle trajectories. In a purely thermal homogeneous system, an MSD that scales linearly with time indicates diffusive motion through a viscous fluid, with the prefactor establishing the particle diffusivity. An MSD that scales subdiffusively ($\sim t^\alpha$, $\alpha < 1$) can instead indicate a viscoelastic medium with characteristic power-law scaling α [15], as well as other possible mechanisms [16, 17]. This analysis has been employed in a number of cellular systems, establishing diffusive behavior in the case of some protein-sized particles [18–20], and subdiffusive dynamics for vesicles and similar-sized exogenous probes in the cytoplasm [12, 15, 21, 22]. An alternate recent approach focuses instead on the velocity auto-correlation function, with negative correlations that decay as a power-law in time taken to be a sign of viscoelastic rheology [16, 23, 24]. Still other studies analyze the distribution of individual step sizes over short time-intervals [7, 25, 26].

All of these approaches are confounded by a number of complications in the intracellular environment [27]. First and foremost, the prevalence of active forces with many different correlation timescales implies that individual particle trajectories cannot be directly related to the rheology of the medium [6]. Furthermore, heterogeneity in the intracellular medium indicates the existence of spatially varying diffusivities [19, 28] and is thought to be responsible for the broad non-Gaussian distribution of step sizes observed for many particles [25, 26, 29]. Nevertheless, extracting the effectively diffusive or subdiffusive behavior of intracellular particles, albeit over a finite range of timescales, can give insight into functionally important consequences such as particle search times, kinetics, or interaction frequencies.

In certain cases it is possible to disentangle the underlying particle dynamics and the effects of forces, flows, or confinement from the measured particle trajectories. For example, when particles are driven by slowly-varying fluid flows overlaid on top of diffusive behavior, the raw MSD appears super-diffusive. However, the diffusive behavior can be extracted by subtracting out a smoothed trajectory and analyzing the resulting MSD curves with an appropriate rescaling [8]. In other cases, separate measurement of the confounding factors is necessary. For instance, active microrheology measurements of cytoplasmic material properties enable 'passive' particle trajectories to then be used for extraction of the spectrum of forces driving particle motion [6]. Mapping out the underlying surface on which a particle is confined and measuring distances along that surface has been shown to enable accurate characterization of diffusing particle dynamics [30].

Confinement effects are a common source of complication in analyzing the trajectories of intracellular particles. Confinement in a finite region can result in apparently subdiffusive MSD curves, on time scales up to an order

* ekoslover@ucsd.edu

of magnitude shorter than the typical time to traverse the confining region [31]. Similarly, velocity autocorrelation functions for particles in confinement exhibit negative peaks that increase when the velocity is measured across longer time intervals [16]. In this manuscript, we focus on how to decouple confinement from the underlying particle dynamics in the case of particles moving along tubular networks.

Eukaryotic cells contain a number of structures that result in confinement of particles at different length scales. The extent of the cell itself provides an upper limit for confinement. Furthermore, many particles are embedded in the membrane or interior of organelles that offer confinement on a subcellular scale. One example of interest is the reticulated mitochondrial network formed in many cell types. These networks exhibit varying connectivity that can be tuned by genetic perturbation of the proteins responsible for mitochondrial fusion and fission [32]. Another organelle with a networked morphology is the endoplasmic reticulum (ER), whose functional roles include lipid distribution, calcium buffering, and protein processing, sorting, and quality control [33, 34]. The ER forms an interconnected system of tubules and stacked sheets, with a continuous lumen and membrane, that spans throughout the cell [35, 36]. Away from the cell nucleus, the ER can be approximated as a tubular network with largely three-way junctions, through which proteins destined for secretion must move in order to encounter the point-like ER exit sites [37–39].

Mathematical models of transport within the ER and mitochondrial networks indicate that the network morphology has the potential to alter search rates and kinetics for proteins to find each other and specific targets within the network [32, 40, 41]. However, examining the interplay between network architecture and kinetics requires an assumed physical model for particle motion (*eg:* diffusive [32, 40], subdiffusive [42], or locally persistent [5, 43]) and an accurate parameterization of that model. Thus, precise empirical quantification of particle dynamics within reticulated networks is of growing interest for elucidating the structure-function relationship of these critical cellular organelles.

Most prior studies on the movement of ER membrane and luminal proteins have focused on bulk measurements of protein spread, including FRAP analysis [44–46] and the spatiotemporal quantification of spreading from a locally photoactivated region [5, 47]. However, it has recently become possible to track the movement of individual proteins through the ER tubules, enabling new observations of dynamics within the ER. For example, single particle trajectories of ER luminal proteins have been found to exhibit unexpectedly fast motion along individual tubes, followed by trapping at junctions – an effect that has been attributed to putative luminal flows over short timescales [5]. ER membrane protein trajectories, however, do not appear subject to these rapid motions. Nevertheless, the analysis of such trajectories is complicated by their confinement within the peripheral ER network structure.

In this work we present a novel method for analysis of diffusive particle trajectories that are confined within a spatial network, consisting of tubules connected by narrow junctions. Namely, we describe how such trajectories can be 'unraveled' to establish a properly sampled underlying trajectory that describes the motion of an identical particle on an infinite line. This unraveling process allows the accurate extraction of a diffusion coefficient for the particle motion by removing the confounding effects of the network structure itself. The procedure is generally applicable to analysis of any locally one-dimensional trajectories where the confining network architecture can be separately imaged. Thus, for example, it can be applied to particles moving along a single finite-length tube, or along a spine-studded morphology such as that found in neuronal dendrites [48, 49].

We validate the method using simulations of particles diffusing on a network, and demonstrate that the technique can differentiate between particles undergoing Brownian versus fractional Langevin motion (a common model for subdiffusion due to viscoelastic rheology [27, 50]). The technique is then applied to the analysis of membrane protein trajectories in the ER, showing that these trajectories are indeed consistent with diffusive motion and providing an estimate of their diffusion coefficient.

Overall, the work presented here enables quantitative analysis of particle trajectories confined on network structures, allowing for mathematically accurate decoupling of confinement effects from the underlying particle dynamics.

II. RESULTS

A. Simulating diffusive particles on a network

We begin by simulating the behavior of diffusive particles on a tubular network. Individual narrow tubules are treated as effectively one-dimensional segments, joined together at point-like junctions. The network structure is thus idealized as a set of nodes connected by edges with well-defined length: ℓ_m for the m^{th} edge. The edges are not necessarily straight, so that ℓ_m can be longer than the spatial distance between two adjacent nodes.

Several algorithms are possible to simulate the trajectory of a diffusive particle on such a network. In recent work, we demonstrated an exact kinetic Monte Carlo algorithm that employs analytical propagator functions obtained by solving the diffusion equation in the neighborhood of each node [41]. By sampling transition times from these functions, the particle can be propagated between adjacent nodes as a continuous-time random walk, with no discretization artifacts. Here, we take an alternate approach, which starts from a diffusive particle trajectory $z(t)$ on an infinite line and maps it probabilistically onto a corresponding trajectory $(m(t), x(t))$

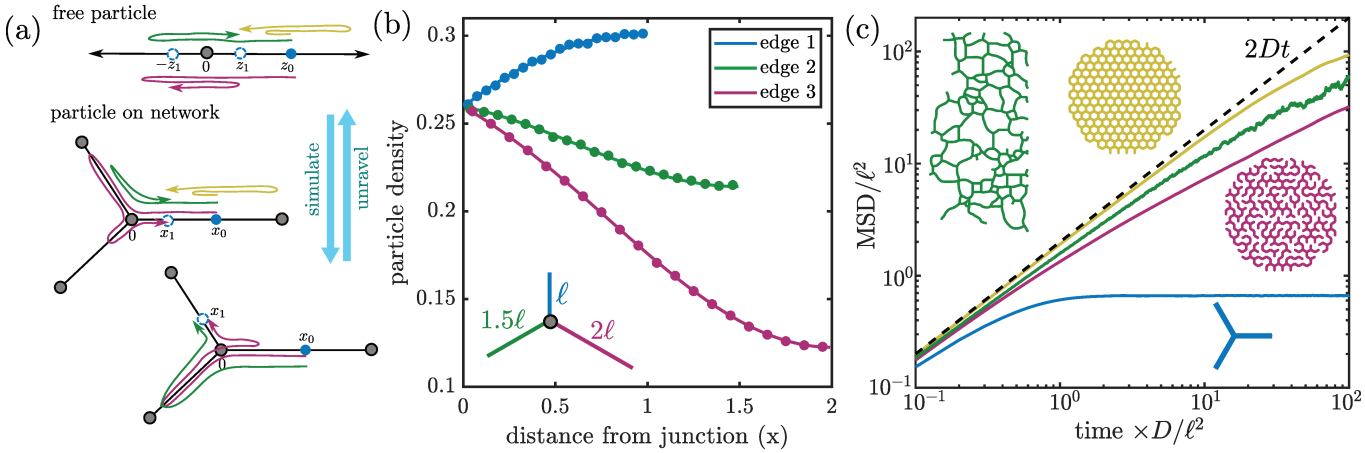

FIG. 1. Simulation of diffusive particle trajectories on a network. (a) Schematic of diffusion simulation and unraveling algorithm. Top: example single-step trajectories starting at z_0 on an infinite line; Bottom: sample corresponding trajectories along the network. Trajectories that pass the node can land on either the same or a different edge. (b) Simulations of particle trajectories using the discrete time propagation algorithm (dots) reproduce exact analytic distributions (lines) on a triskelion network. Densities are shown for a particle starting at the center node, propagating for a total time $t = 0.8\ell^2/D$. (c) Diffusive particle mean squared displacement depends on the structure of the confining network. Dimensionless MSD is shown for particles on a triskelion geometry (blue), a honeycomb network of diameter 15ℓ (yellow), a honeycomb with 30% of its edges removed (purple), and a section of a peripheral ER network extracted from a COS7 cell (green). Dashed black line shows linear scaling. Length units are scaled by the average network edge length (ℓ) and time units by ℓ^2/D.

on the network (where m is a network edge index and x is the position along the edge). In a subsequent section, we demonstrate how this mapping can be reversed to extract the underlying diffusive dynamics of a particle whose motion is observed on a network of known structure.

Consider a discretized trajectory $\{z_i\}$ of a free Brownian particle with diffusivity D, evaluated at discrete times $t_i = i\Delta t$. The increments of such a trajectory are distributed according to a normal distribution: $\Delta z \sim \mathcal{N}(0, \sqrt{2D\Delta t})$. To map this trajectory onto an equivalent particle diffusing over the network structure, we use these increments Δz for propagation on the network. In particular, we assume that each time the diffusing particle passes a network node, it selects uniformly at random the next edge from the ones attached to that node. Thus, a reversal in the trajectory z_i on an infinite line will always correspond to a reversal on the network, but additional reversals at a network node may also occur that are not apparent on the infinite line (*e.g.:* green path, Fig. 1a).

Our approach assumes that the discrete time step is short enough that on any single step the particle can pass only the network node that is closest to its starting position (in terms of distance along the edge). Specifically, we assume that $|\Delta z| < \ell_m/2$ for the current edge m on which the particle is located.

To map an unconstrained trajectory step Δz onto the network (Fig. 1a), consider a particle starting at position x_0 along edge m, and assume that $x_0 < \ell_m/2$, so that the particle is closer to the first node of the edge. We want to find the next position x_1 for the particle, given its sampled trajectory on the infinite line. If $\Delta z < -x_0$ then the particle trajectory must have passed the node during this time step. We then place the particle at position $x_1 = |x_0 + \Delta z|$ on an edge selected uniformly at random from among all the edges attached to that node (including the original edge). If $\Delta z > -x_0$ then the particle may also have passed the node during that time step. The probability that it has done so can be computed as

$$p_{\text{pass}} = \exp\left[-\frac{(x_0 + \Delta z)x_0}{D\Delta t}\right], \tag{1}$$

(see Appendix A 1 for derivation). If it passed the node, then it can end the time step on any of the adjacent edges with equal probability; if it did not pass the node then it must still be on its original edge. The subsequent position of the particle is then given by $|x_0 + \Delta z|$ with probability $1 - p_{\text{pass}} + p_{\text{pass}}/d$ of landing on its original edge and probability p_{pass}/d of landing on each of the other adjacent edges, where d is the degree of the node. The propagation of the particle is then repeated from its new position. If the particle originates close to the other end of the edge ($x_0 > \ell_m/2$) then an analogous calculation is performed by considering the nearby node on the far end of edge m.

It should be noted that this algorithm also handles reflections off of a dead-end node. Increments that would lead an unconstrained particle to pass such a node simply result in the particle being placed back upon the single edge leading to the dead-end. Such explicit reflections are typically implemented in Brownian and fractional Brownian dynamics simulations with hard-wall boundaries [51].

The proposed algorithm accurately represents the behavior of a continuously diffusing particle over the time step Δt so long as we can neglect any trajectories that pass a node other than the most nearby one over the course of a single time step. Therefore, unlike the exact algorithm described in previous work [41] it requires the constraint $\sqrt{2D\Delta t} \ll \ell_m$. In Fig. 1b, we demonstrate that for small Δt the agent-based simulations described here accurately reproduce analytically computed particle distributions in a simple triskelion network (see Appendix A 2).

B. Network confinement modulates particle MSD

A traditional metric for analyzing particle trajectories is to look at the mean squared displacement (MSD), defined by

$$\mathrm{MSD}(t) = \left\langle |\vec{r}(t) - \vec{r}(0)|^2 \right\rangle, \tag{2}$$

where $\vec{r}(t)$ gives the spatial position of the particle at time t, and the average is taken both over time and over an ensemble of many particles. Particles that diffuse unimpeded on an infinite linear domain exhibit the relationship $\mathrm{MSD} = 2Dt$. Identical behavior is observed for particles diffusing on a network comprising an infinite lattice of tubules. The effect of confinement in a finite domain is a well-known complication of MSD analysis [31], with the MSD beginning to flatten on time scales comparable to $\sqrt{R^2/2D}$ for a domain of radius R (Fig. 1c).

When the connectivity of the network structure is reduced below that of the well-connected lattice, the time dependence of the mean squared displacement flattens still further. In Fig. 1c (purple curve), we show the MSD of particles on a diluted honeycomb network with 30% of its edges removed in such a way as to maintain a single connected component. The MSD shows an apparently subdiffusive (sublinear) scaling with time, as missing connectivity and an abundance of dead ends forces particles to take much longer paths to get from one part of the network to another.

Cellular organelle networks, such as the peripheral endoplasmic reticulum and mitochondrial network structures, also show reduced connectivity, with dead-end nodes and heterogeneous pore sizes between connected edges. In Fig. 1c (inset) we show a section of network extracted from an image of the peripheral ER in a mammalian cell. Simulating diffusive particle trajectories on the extracted section of an ER network indicates that the MSD is also expected to scale sublinearly with time (Fig. 1c, green curve).

We note that the dead-end nodes along the boundary of the extracted ER network arise from a combination of the cell boundary and the finite field of view captured via high-resolution imaging. In Supplemental Material Section S1, we show that the results shown here are unaltered if simulated trajectories are truncated whenever they touch the dead-ends at the edge of the imaging area, analogous to the termination of experimental trajectories whenever a particle leaves the field of view.

These simulations highlight the inherent difficulty of quantifying particle diffusivity on a network by analyzing the mean squared displacement of observed trajectories. Namely, the MSD convolves together two separate effects: the underlying dynamics of the moving particles and the morphology of the network within which they are confined. We thus proceed to develop a method for separating out these two effects and extracting particle diffusivity from their behavior on a known network structure.

C. Unraveling diffusive trajectories on networks

To unravel the particle dynamics from the network architecture, we proceed by inverting the algorithm used to map the discrete trajectory of an unconfined particle ($\{z_i\}$) onto a trajectory over the network (Fig. 1a). Given a set of discrete 2D (or 3D) observations of the network-confined particle ($\{\vec{r}_i\}$), we seek to find the trajectory that particle would have taken if allowed to move over an infinite line. To begin, we re-express the spatial trajectory in terms of network coordinates $\{m_i, x_i\}$ that list the edge m_i and position along that edge $x_i \in (0, \ell_i)$ of the particle at time point t_i. We then consider the start and end positions of the particle at each time-step, assuming that there is an underlying free one-dimensional trajectory such that z_i, z_{i+1} were mapped to network positions $(m_i, x_i), (m_{i+1}, x_{i+1})$ using the algorithm described in the previous section.

For sufficiently small time-steps, we can again assume that the particle could only have passed over the node closest to x_i. Without loss of generality, we take this node to be the one located at position 0 on edge m_i. For simplicity of notation, we shift the unconstrained trajectory such that $z_i = x_i$. The next observed position of the unconstrained particle must then be $z_{i+1} = \pm x_{i+1}$. Bayes' rule [52] allows calculation of the probability associated with each choice, conditional on the observed particle positions. The probability that the unconstrained trajectory ended at $z_{i+1} = x_{i+1}$ after the time-step, given that the particle ended at (m_{i+1}, x_{i+1}) on the network is:

$$p_+ = \mathcal{P}(z_{i+1} = x_{i+1} | m_{i+1}, x_{i+1}) = \frac{\mathcal{P}(m_{i+1}, x_{i+1} | z_{i+1} = x_{i+1}) \mathcal{P}(z_{i+1} = x_{i+1})}{\mathcal{P}(m_{i+1}, x_{i+1})} \tag{3}$$

The free particle increments are sampled from a normal distribution, so that

$$\mathcal{P}(z_{i+1} = \pm x_{i+1}) = \frac{1}{\sqrt{4\pi D \Delta t}} e^{-\frac{(x_i \mp x_{i+1})^2}{4D\Delta t}}. \tag{4}$$

If the particle moved on to a different edge ($m_{i+1} \neq m_i$), then the unconstrained trajectory must have passed

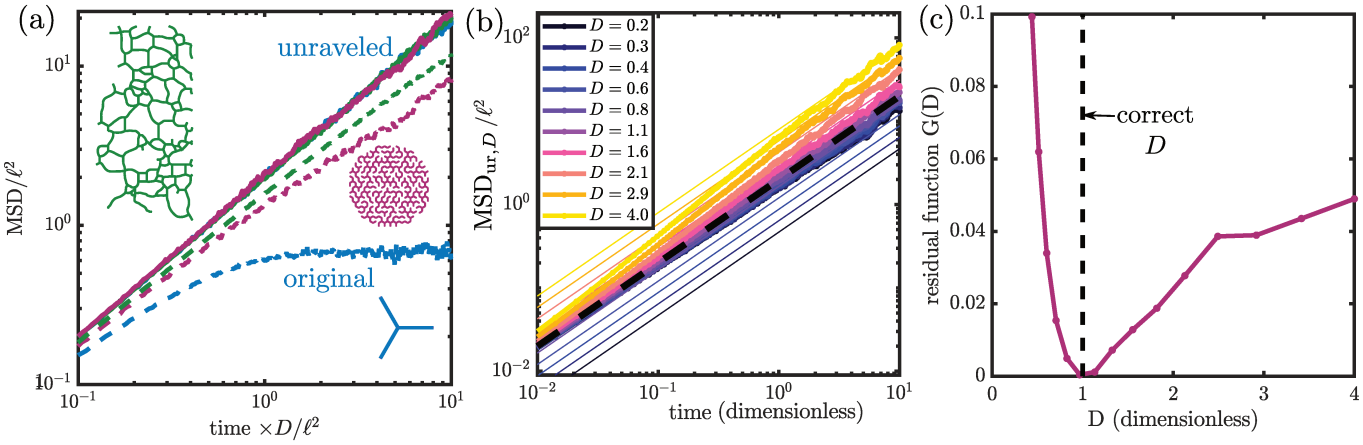

FIG. 2. Unraveling simulated trajectories to estimate diffusivity. (a) Dimensionless MSD of particle trajectories on a triskelion (blue), a decimated honeycomb network (purple), and a segment of peripheral ER (green). All simulations were run with $D = 1$. Original MSD (from Fig. 1c) is shown with dashed lines, MSD after unraveling (with $D = 1$) shown with solid lines. (b) MSD of trajectories on decimated honeycomb network, unraveled using different values of the diffusion coefficient D (thick lines), compared to the expected $2Dt$ (thin lines). Dashed black line indicates values for the correct diffusion coefficient. All units are non-dimensionalized by the edge length and the simulated diffusivity. (c) Residual function $G(D)$ plotted for the different diffusion coefficient values used in unraveling. Dashed line shows the correct $D = 1$ used in the simulation, which matches well to the minimum of the residual function.

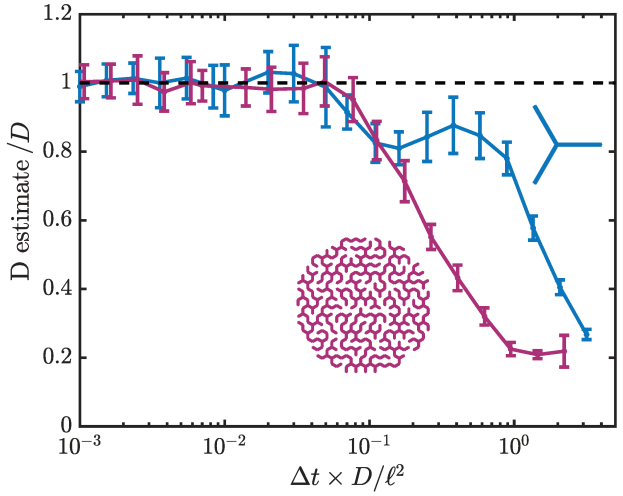

FIG. 3. Diffusion coefficient estimates for different timesteps. Simulated trajectories on a diluted honeycomb network (purple) and a triskelion network (blue) are unraveled to obtain an estimated D value. Each analysis involves 100 independent trajectories of 100 time steps each. Error bars give standard deviation from 20 replicate analyses. All values are non-dimensionalized by the edge length ℓ and the simulated diffusivity D.

zero and the conditional probabilities of the observed end-point on the network are:

$$\mathcal{P}(m_{i+1}, x_{i+1}|z_{i+1} = x_{i+1}) = \frac{1}{d} e^{-\frac{x_i x_{i+1}}{D\Delta t}}, \tag{5}$$

$$\mathcal{P}(m_{i+1}, x_{i+1}|z_{i+1} = -x_{i+1}) = \frac{1}{d}. \tag{6}$$

The first line gives the probability that the unconstrained trajectory passed 0 (as in Eq. 1) before returning to the positive side. The second line simply indicates that if the unconstrained trajectory ends on the negative side, it must have passed zero and is thus equally likely to be mapped to any of the adjacent edges.

For a particle that ends on the same edge as its starting point ($m_{i+1} = m_i$), the conditional probability given $z_{i+1} = x_{i+1}$ is altered to

$$\mathcal{P}(m_{i+1}, x_{i+1}|z_{i+1} = x_{i+1}) = 1 + \left(\frac{1}{d} - 1\right) e^{-\frac{x_i x_{i+1}}{D\Delta t}}, \tag{7}$$

which includes an additional term for unconstrained particles that never pass the origin.

Plugging into Bayes' rule (Eq. 3) results in the following probabilities for the end-point of the unconstrained trajectory:

$$p_+ = \begin{cases} \frac{1}{2}, & m_{i+1} \neq m_i \\ \frac{1}{2-d+d\exp(x_i x_{i+1}/D\Delta t)}, & m_{i+1} = m_i. \end{cases} \tag{8}$$

The conditional probability p_- that $z_{i+1} = -x_{i+1}$ given the observed values of m_{i+1}, x_{i+1} can be computed as $p_- = 1 - p_+$.

For the network trajectory $\{m_i, x_i\}$, we obtain an 'unraveled' trajectory $\{z_i\}$, by sampling the next position at each step according to Eq. 8, considering only the node closest to x_i for potential passage by the unconstrained particle. The mean squared displacement and velocity autocorrelation function for the unraveled trajectory can then be analyzed in the usual manner. As shown in Fig. 2a, the unraveled trajectory mean squared displacement (MSD_{ur}) for simulated particles diffusing

on a network regains its linear time scaling, with the correct prefactor: $\mathrm{MSD}_{\mathrm{ur}} = 2Dt$.

Computing the unraveled trajectories requires knowledge of the particle diffusion coefficient D in order to correctly sample the step direction from Eq. 8. Since one of the primary goals of the unraveling procedure is to gain an estimate of particle diffusion coefficient, D cannot be assumed *a priori*. Instead, the unraveling process is performed with a range of different diffusivities to find a self-consistent value. Values of D that are too large or too small result in an unraveled MSD that deviates from the expected behavior (Fig. 2b). We estimate the underlying particle diffusion coefficient by finding the value of D that minimizes the difference between the computed $\mathrm{MSD}_{\mathrm{ur}}(t; D)$ and $2Dt$.

We assess the goodness of fit on a log-log scale, as plotted in Fig. 2b. Specifically, we perform a logarithmic transform of both axes and compute $G = 1 - R^2$, where R^2 is the coefficient of determination used to assess the accuracy of the linear model [53]. This metric is computed for each value of diffusivity D as:

$$G(D) = \frac{\sum_i \log^2\left[\mathrm{MSD}_{\mathrm{ur}}(t_i|D)/(2Dt_i)\right]}{\sum_i \log^2\left[\mathrm{MSD}_{\mathrm{ur}}(t_i|D)/\left\langle \mathrm{MSD}_{\mathrm{ur}}\right\rangle_t(D)\right]} \qquad (9)$$

where the residuals are evaluated at logarithmically spaced time points t_i and $\langle \mathrm{MSD}_{\mathrm{ur}}\rangle_t$ refers to the average value over all time-points. The final diffusion coefficient estimate is the value of D that minimizes $G(D)$ (Fig. 2c). Obtaining an accurate estimate of the diffusion coefficient via this method requires a sufficient number and length of trajectories input into the time- and ensemble-average when calculating the unravelled MSD curves. The effect of trajectory length and ensemble size on the estimated diffusivity is shown in Supplemental Figure S2.

Figure 3 shows how the estimated diffusion coefficient varies with the time-step of the trajectory. Our approach is valid only if the time-step is small enough that individual consecutive snapshots are very unlikely to involve the particle trajectory passing any network node other than the one nearest to the particle. During the analysis, any steps that involve the particle jumping onto a non-adjacent edge result in breaking the trajectory up into separate segments. For larger step-sizes (roughly, $\Delta t \gtrsim 0.1\ell^2/D$), such large steps become increasingly common. Breaking the trajectory then results in a systematic underestimate of the diffusion coefficient since large steps are removed from the analysis. Thus, in order to accurately assess particle dynamics on a network, the particle positions must be visualized rapidly enough that the particle passes no more than one node on each step.

D. Fractional Langevin motion and velocity autocorrelations

An important application of MSD analysis for single particle trajectories is to elucidate the relevant dynamic model that best describes their behavior[7]. In particular, particles that exhibit an MSD scaling linearly with time are generally assumed to be moving in an effectively diffusive manner. By contrast, subdiffusive scaling ($\mathrm{MSD} \sim t^\alpha$ for $0 < \alpha < 1$) can be explained by a number of underlying physical models, including continuous time random walks, confinement, and fractional Langevin motion (fLM) [16, 17]. Fractional Langevin motion is expected for particles subject to thermal fluctuations in a viscoelastic medium, driven by fractional Brownian forces with a power-law correlation over time that scales as $t^{-\alpha}$[51, 54]. The fLM model, with sublinear scaling exponent $\alpha < 1$, has been shown to be relevant for a variety of cytoplasmic and intranuclear particles [23, 24, 26, 55]. For particles moving on a network, it can be difficult to distinguish microscopic subdiffusion arising from fLM dynamics versus effective subdiffusion on longer scales due to the network confinement. We here consider whether our analysis method can help accurately determine whether one or the other of these common dynamic models is a better descriptor of the microscopic dynamics of observed network-confined particles.

To simulate the dynamics of a particle undergoing fLM on a network, we first generate fractional Brownian forces in two dimensions (2D) using previously established methods [50, 56]. Particle step increments in 2D are then computed by convolving the past history of steps with the appropriate power-law memory kernel, followed by zeroing out of the step component perpendicular to the current edge axis (details in Appendix A 4). The overall approach is analogous to that used for simulating the fractional Langevin equation in a confined geometry [51], in the limit of no inertia and narrow edge confinement.

As expected, the simulated trajectories exhibit an MSD that scales as a power-law with time, $\mathrm{MSD} \sim t^\alpha$ (Supplemental Material, Fig. S3). These subdiffusive trajectories can be unraveled as described in the previous section, to remove the effect of network confinement. The unraveling procedure assumes diffusive transport when computing node passage probabilities, and attempts to unravel with different values of the trial diffusivity D until a self-consistent value is found. Because the underlying motion is in fact not diffusive in this example, the resulting unraveled MSD curves are notably deformed (Fig. 4a). Consequently, the residual metric (comparing to a linear, diffusive scaling) is substantially higher for these trajectories, serving as an indicator of non-diffusive transport (Fig. 4a, inset).

An alternative approach for distinguishing fLM from diffusive trajectories on a network involves analysis of the velocity autocorrelation function for the unraveled trajectories. For velocities computed over time-interval δ, the autocorrelation function is defined by [57]

$$C_v^{(\delta)}(t) = \frac{1}{\delta^2}\left\langle [x(t+\delta) - x(t)] \cdot [x(\delta) - x(0)]\right\rangle, \qquad (10)$$

where the average is taken over both time and the particle

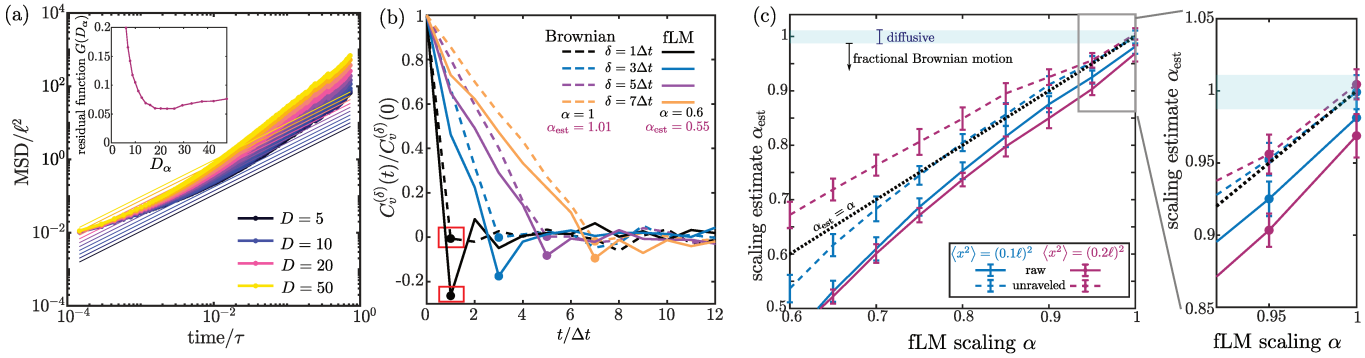

FIG. 4. Distinguishing Brownian motion versus fLM from unraveled particle trajectories on a diluted honeycomb network. (a) MSD of fLM trajectories unraveled with different trial values of D (thick lines). Thin lines show $2Dt$ for each trial value of D. Inset shows residual function $G(D)$, showing how no trial D gives a good correspondence with the expected diffusive scaling. Simulations used scaling exponent $\alpha = 0.6$, with prefactor set such that individual step sizes are comparable to the Brownian simulations in Fig. 2, with $2D_\alpha \Delta t^\alpha = (0.1\ell)^2$. Length and time units are non-dimensionalized by ℓ and $\tau = (\ell^2/D_\alpha)^{1/\alpha}$, respectively. (b) Normalized velocity autocorrelations for unraveled trajectories of simulated particles undergoing Brownian motion (dashed lines) and fLM with $\alpha = 0.6$ (solid lines). Red box indicates first negative peak, used to extract estimated scaling exponent $\alpha_{\rm est}$. (c) Estimated scaling exponent for simulated fLM particles with different true values of α. Estimations are shown based on the velocity autocorrelation of either raw 2D trajectories (solid) or unraveled 1D trajectories (dashed). Simulations were carried out with two different root mean squared step sizes: 10% (blue) and 20% (purple) of the network edge length. All simulations included 100 particles tracked for 100 time steps. Error bars are standard deviations from 50 independent replicates. Cyan region indicates the range of $\alpha_{\rm est}$ that should be taken to imply purely diffusive motion, obtained as average ± standard deviation for Brownian particle simulations. Right: zoomed-in section shows that network confinement makes Brownian particles ($\alpha = 1$) appear to have a lowered estimated scaling ($\alpha_{\rm est} < 1$), whereas unraveled trajectories show the correct Brownian exponent $\alpha_{\rm est} = 1$.

ensemble. This function exhibits a negative peak at $t = \delta$, rising back towards zero in a polynomial fashion for $t > \delta$. The normalized negative peak $C_v^{(\delta)}(\delta)/C_v^{(\delta)}(0)$ becomes deeper for more subdiffusive motion (lower α) and, for fractional Langevin motion, is independent of the choice of window size δ in defining the velocity[16, 23, 24]. The scaling exponent α can be extracted directly from this value according to the expression [57]:

$$\left| \frac{C_v^{(\delta)}(\delta)}{C_v^{(\delta)}(0)} \right| = 1 - 2^{\alpha - 1}. \tag{11}$$

We plot the normalized velocity autocorrelation for unraveled trajectories of Brownian particles and particles undergoing fLM in Fig. 4a,b. For Brownian particles, the velocity correlations are flat for $t > \delta$, emphasizing that the unraveling procedure removes the effect of confinement and dead-ends in the network, which would be expected to yield negative peaks [16]. For particles undergoing fLM, the unraveling decreases the magnitude of the negative peaks at larger step-sizes, consistent with the turning upward of the MSD curves for these trajectories. However, the form of the velocity autocorrelation function is still clearly non-diffusive, demonstrating that this metric can be used to diagnose fLM versus Brownian motion on a network.

To generate an estimate of the fLM scaling exponent, we use Eq. 11 at $\delta = \Delta t$ (a single trajectory step). As shown in Fig. 4c, unraveled trajectories of simulated Brownian particles on a network give an accurate estimate of $\alpha_{\rm est} \approx 1.01 \pm 0.01$ (mean ± standard deviation) based on the first negative peak in the velocity autocorrelation functions. When the same analysis is applied to simulated fLM trajectories with $\alpha = 0.6$, the unraveling procedure gives a biased estimate of the scaling exponent ($\alpha_{\rm est} = 0.54 \pm 0.025$), but still clearly differentiates between fLM and Brownian motion. Simulations of fLM with a range of different scaling exponents (Fig. 4c) indicate that accurate estimates of the scaling exponent can be obtained for $\alpha \gtrsim 0.75$, when individual step sizes are set to 10% of the network edge length. For larger step sizes, this approach overestimates α, due to the bias towards diffusive motion introduced in the unraveling process whenever the particle passes a node. However, particles undergoing fLM still yield an estimated $\alpha_{\rm est}$ that is significantly less than 1, allowing the trajectories to be distinguished from those of Brownian particles. By contrast, if the velocity autocorrelation is analyzed for raw trajectories confined on a network, then even Brownian particles ($\alpha = 1$) are likely to yield an estimated scaling value $\alpha_{\rm est}$ that is below the expected range (shaded region in Fig. 4c). Thus, network confinement can make Brownian motion appear as fLM, and the unraveling procedure removes this confounding effect. Notably, more rapid high-resolution imaging that can yield even smaller observed step sizes would allow for a more accurate estimate of the scaling exponent for particles undergoing fLM.

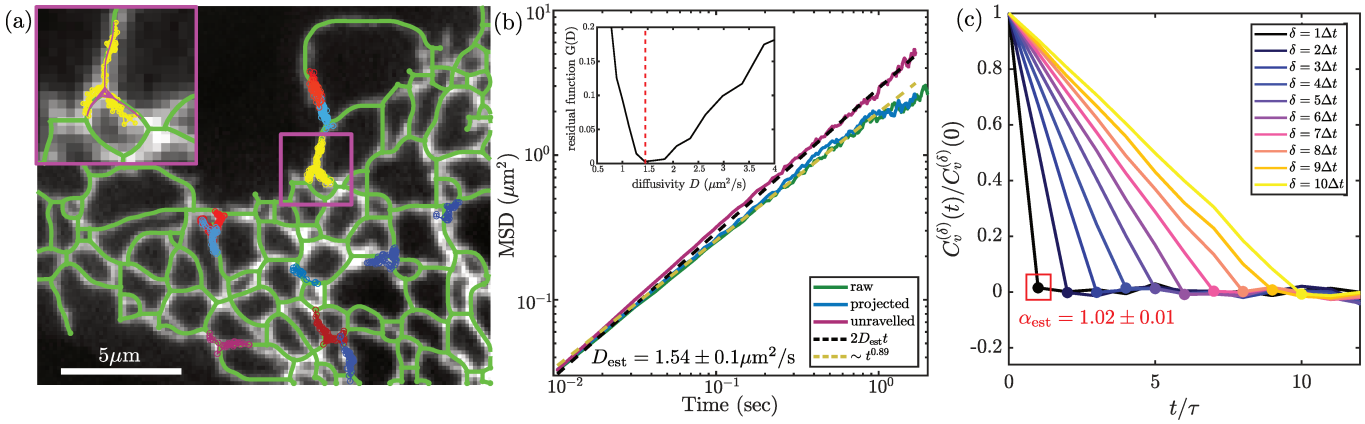

FIG. 5. Unraveling of membrane protein (Halo-TA) trajectories in the peripheral ER networks of an example COS7 cell. (a) Extracted network structure (green) superimposed on a confocal image with fluorescently labeled ER marker. Trajectories within 1 sec of this snapshot are shown as colored circles. Inset shows single trajectory, projected onto network edges (magenta). (b) Ensemble-averaged MSD for raw trajectories (green), projected trajectories (blue), and unraveled trajectories (purple). Dashed magenta line indicates apparent subdiffusion for particle trajectories due to confinement in network structure. Dashed black line shows linear scaling with the estimated diffusion coefficient. Inset: residual function for unraveling with different diffusivity values, with self-consistent estimate marked in red. (c) Normalized velocity autocorrelation for unraveled trajectories, with estimated scaling exponent $\alpha_{\rm est}$ is obtained from the first negative peak. Errors for $D_{\rm est}$ and $\alpha_{\rm est}$ are standard deviations obtained from bootstrapping over individual unraveled trajectories.

E. Application to membrane proteins on ER tubules

As a direct application of this methodology to experimental data, we consider single particle trajectories of a model ER transmembrane protein (a HaloTag fused to the minimal targeting domain of Sec61b, Halo-TA), moving along the peripheral ER tubules of COS7 cells.

The peripheral ER of COS7 cells provides a convenient example system consisting of a pseudo-planar network of narrow tubules. The diameter of ER tubules has previously been measured at approximately 100nm in this cell type [58–60]. The average edge length between 3-way junction nodes in our extracted network structures is $1.2 \pm 0.76\mu$m (see Supplemental Material, Section S4), comparable to previous measures of ER edge length in COS7 cells [41]. While the diameter of COS7 cells in culture can be above 50μm (e.g., [59, 60]), we focus on smaller $\sim 15\mu$m regions, where the peripheral network morphology is well-resolved (Fig. 5a).

The effective diffusivity of the Halo-TA proteins is the target quantity we aim to extract through the unraveling algorithm. Prior bulk measurements of the spreading of a photoactivated membrane marker in the peripheral ER network indicate an approximate value of $D \approx 1.8\mu\text{m}^2/\text{s}$ [47].

Widefield images of the ER network as well as individual fluorescently labeled Halo-TA proteins were collected simultaneously with rapid time resolution ($\sim$ 100 Hz). Because ER networks are dynamic, rearranging over tens of seconds [61–64], peripheral network structures were extracted at 1 second intervals to serve as the underlying domain geometry for the particle trajectories. Details on imaging, image analysis, and particle tracking methods are provided in the Methods section (Appendix A).

For each network structure, trajectory segments collected within ± 1 sec of the corresponding image time were mapped onto the network by projecting to the nearest point along the edges (Fig. 5a). All projected trajectories imaged within a given cell (corresponding to approximately 1 minute total imaging time) were then collected together for analysis. As seen in Fig. 2b, both the raw and projected trajectories exhibited an apparently subdiffusive MSD scaling with time, as expected for simulated diffusive particles on a sample ER network (Fig. 1c). The close correspondence between raw and projected trajectories indicates that the proteins were in fact largely confined to the visible ER tubules, with most of their motion occuring along the tubule axis. In Supplemental Material (Figure S6) we explore further the effect of particles moving along the circumference of the ER tubules rather than directly along the axis. We show, using simulations, that the narrow 50 nm radius of ER tubules [58] implies that these perpendicular particle displacements will not significantly affect the analysis.

Projected trajectories were unraveled as described in Section II C to extract the underlying free-particle dynamics. The mean squared displacement $\text{MSD}_{\rm ur}$ of the unraveled trajectory closely matched the expected $2D_{\rm est}t$ behavior (Fig. 5b) with a diffusion coefficient of $D_{\rm est} = 1.54 \pm 0.1\mu\text{m}^2/\text{s}$, where the standard deviation in the estimate is obtained by bootstrapping over individual particle trajectories. The velocity autocorrelation function of the unraveled trajectories is consistent with the expected behavior for diffusive particles, showing very little correlation for $t > \delta$ (Fig. 5c). Estimating the scal-

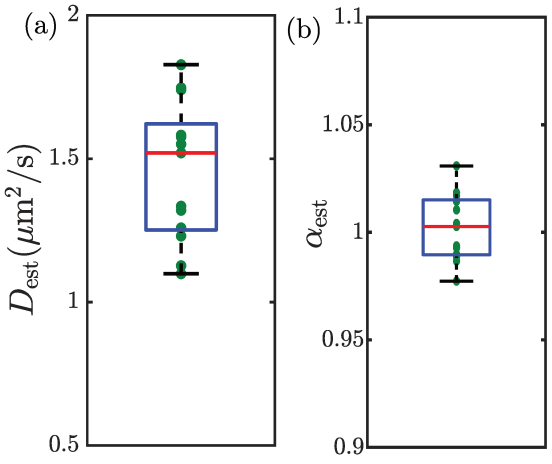

FIG. 6. Analysis of trajectories for Halo-TA ER membrane proteins from multiple COS7 cells. (a) Estimated diffusion coefficient $D_{\rm est}$. (b) Estimated scaling exponent $\alpha_{\rm est}$. $N = 13$ independent cells were analyzed.

ing exponent α from these velocity autocorrelations (as described for simulated trajectories above) yields a value of $\alpha_{\rm est} = 1.02 \pm 0.01$, with standard deviation again obtained by bootstrapping.

The analysis was repeated for particle trajectories and network structures obtained from 11 different cells (Fig. 6), with resulting diffusion coefficient estimates $\langle D \rangle = 1.45 \pm 0.24 \mu{\rm m}^2/{\rm s}$ (mean $\pm$ standard deviation). The extracted diffusion coefficient is similar to values recently estimated from bulk measurements of photoactivated protein spreading in the ER [47]. The scaling estimates from the velocity autocorrelation of unravelled trajectories in each cell yielded $\langle \alpha \rangle = 1.00 \pm 0.02$ (standard deviation across cells), consistent with diffusive motion of the Halo-TA ER membrane protein.

We note that, given our diffusion coefficient estimate and average ER edge length (Supplemental Fig. S4), we would expect the unraveling procedure to be accurate for step sizes $\Delta t \lesssim 0.07$sec, a condition which is satisfied by the 100Hz imaging rate.

III. DISCUSSION

Traditional approaches to quantifying single particle trajectories involve using the mean squared displacement or velocity autocorrelation function to characterize the diffusive or subdiffusive motion of the particles. However, for particles trapped inside the complex spatial geometry of intracellular structures, these approaches are confounded by the effects of confinement. Such effects can make diffusive motion appear subdiffusive and lead to underestimation of the particle motility. In this study, we demonstrate a methodology for decoupling the underlying microscopic diffusion of particles from the effect of spatial confinement using direct observation of the structure, in the specific case of particles confined within a tubular network.

Our approach involves unraveling a particle trajectory on a network by sampling the hypothetical path of that particle if it were to undergo unconstrained diffusion on an infinite line. In classic simulations of a Brownian particle, each step of the particle represents an ensemble of possible paths leading from the starting position to the next one. When all likely paths stay within a single edge of the network, such a classically sampled step remains accurate. However, if there is a non-trivial chance of passing a network junction during that time-step, then it becomes necessary to consider the excursions of the particle to different edges surrounding that junction. We develop an algorithm that makes use of the statistical weighting of these excursions to 'fold' one-dimensional diffusive paths onto the edges around a network junction. This serves as a mathematically accurate method for discrete-time Brownian dynamics simulations of particles along a network of tubules.

We then take a Bayesian approach to inverting this algorithm. Namely, starting with an observed trajectory of discrete steps on a network, we sample the unconfined one-dimensional trajectory that would lead to the observed particle positions. The resulting 'unraveled' trajectories of simulated Brownian particles exhibit all the features of classic Brownian motion and can be analyzed using the usual quantification of MSD and velocity autocorrelations. This approach makes it possible to extract the underlying diffusion coefficient of the particle, as well as to differentiate between diffusive and subdiffusive microscopic motion.

Simulations of particles undergoing fractional Langevin motion on network structures indicate that applying our unraveling algorithm can accurately differentiate such dynamics from Brownian diffusion. For sufficiently small step-sizes, analysis of the velocity autocorrelation function for unraveled trajectories yields an approximate estimate of the fractional scaling exponent α. Furthermore, although raw Brownian trajectories may be effectively subdiffusive at large scales due to confinement within the network, unraveling the trajectories allows for accurate identification of Brownian scaling behavior ($\alpha = 1$) from the velocity autocorrelation function. Hence, the unraveling technique can be used to distinguish large-scale subdiffusion arising from microscopic causes (as in fLM) from the apparent subdiffusion caused by network confinement.

Our proposed approach for uncoupling diffusive transport from network confinement is subject to certain inherent limitations. It is applicable specifically to particles moving on a network of narrow tubules, so that motion along individual edges can be approximated as one-dimensional. It also requires sufficiently frequent observations of the particle position so that each particle can be assumed to pass at most one node junction during each time-step. This is equivalent to requiring that the particle steps be shorter than the typical edge length. Expanding the proposed algorithm to find the correct sta-

tistical weighting for paths that pass multiple nodes over the course of a time-step serves as a promising avenue for future work.

As an example application of the unraveling algorithm, we analyze the trajectories of membrane-bound proteins in the endoplasmic reticulum (ER). The peripheral ER in many cell types forms a tubular network structure, which hosts a variety of proteins that diffuse within its lumen and membrane. Among its many biologically crucial functions, it is thought to serve as an intracellular network for the sorting and delivery of ions, lipids, and secreted proteins. Currently, the mechanism and spatial dynamics of these phenomena are challenging to observe, since the complex structure masks the interpretation of dynamic data collected within the organelle. Quantifying particle motion in the ER is crucial to elucidating the impact of its reticulated structure on the kinetics of biochemical pathways embedded within this organelle. Such studies constitute a first step towards generating a mechanistic understanding of ER-localized biological processes and their regulation.

Trajectories of single transmembrane proteins on mammalian ER networks were collected at a sampling rate of approximately 100Hz, sufficiently rapid to ensure multiple steps of each protein between junction passage events. Traditional analysis of the MSD for raw particle trajectories was confounded by confinement within the network, as indicated by an apparent subdiffusive scaling estimate. However, application of the unraveling algorithm demonstrated that the dynamics of these particles is consistent with classic Brownian motion, with a diffusion coefficient of $D \approx 1.5\mu\text{m}^2/\text{s}$. This estimate is compatible with bulk measurements of protein diffusivity in the ER membrane [47].

Our analysis demonstrates that the specific ER membrane protein studied here does not show signs of fractional Langevin motion on a microscopic scale. Although no proteins exhibiting such dynamics in the ER are known to date, the method described here will make it possible to accurately classify the underlying dynamics as Brownian versus fLM as new data on protein motion in the ER becomes available. Furthermore, we emphasize that the measurements here were limited to a protein embedded in the ER membrane. Past studies have indicated that aqueous proteins in the ER lumen may exhibit non-diffusive motion dominated by rapid processive runs along the tubules [5]. Unraveling the dynamics underlying luminal protein trajectories is left as a topic for future work.

The algorithm proposed here is not specific to protein motion in the ER, but rather is a general mathematical tool for analyzing ensembles of diffusive trajectories on networks embedded in physical space. Such spatial networks have been analyzed in the context of roads, power grids, and venation patterns as well as intracellular structures [65]. In cell biology, mitochondrial networks [32] and the dendritic trees of neurons [49] provide additional examples of network structures where diffusion can play an important role in protein transport. Our focus here is specifically on diffusive dynamics over the network, but the unraveling method also provides a potential tool for diagnosing when particle motion is non-diffusive at the microscopic scale. We show that the method can accurately distinguish whether particle motion is most consistent with fLM or Brownian motion. Future work will pursue the possibility of distinguishing other dynamic behaviors, such as directed flow along edges [5, 43], or continuous-time random walks associated with sporadic binding [66], as well as exploring combinations of these dynamic processes.

Because the unraveling approach provides a quantitative estimate of particle diffusion coefficient, it has potential applications in distinguishing the effect of external perturbations on either network structure or the dynamics of the particles themselves. For example, mutations in ER morphogen proteins can alter the radius of ER tubules [47], or the density of tubule junctions [67]. However, the consequences of these morphological changes on protein diffusivity in the ER remain unclear, and could be approached by unraveling membrane and luminal protein trajectories according to the methods proposed here. Overall, the ability to quantify trajectories by removing the complicating effects of confinement is critical to understanding the behavior of particles trapped in complex reticulated geometries, in cell biology and beyond.

ACKNOWLEDGEMENTS

This work was initiated at the QCB Cell Modeling Hackathon, supported by Wallace Marshall and the Quantitative Cell Biology Network (sponsored by NSF grant MCB1411898). The authors thank Jonathon Nixon-Abell, Zubenelgenubi Scott, and the members of the Hackathon for helpful discussions. They also thank Jonathon Nixon-Abell for collecting and curating some of the data used in this study. Funding for this work was provided by NSF grant MCB-2034482 (EFK), a Cottrell Scholar Award from the Research Corporation for Science Advancement (EFK), a Chancellor Funded Research Grant (EFK), and direct support of the Howard Hughes Medical Institute (CJO and JL-S).

[1] D. Wirtz, Particle-tracking microrheology of living cells: principles and applications, Ann Rev Biophys **38**, 301 (2009).

[2] T. M. Squires and T. G. Mason, Fluid mechanics of microrheology, Annu Rev Fluid Mech **42**, 413 (2010).

[3] J. Elf, G.-W. Li, and X. S. Xie, Probing transcription factor dynamics at the single-molecule level in a living

cell, Science **316**, 1191 (2007).
[4] B. R. Parry, I. V. Surovtsev, M. T. Cabeen, C. S. OHern, E. R. Dufresne, and C. Jacobs-Wagner, The bacterial cytoplasm has glass-like properties and is fluidized by metabolic activity, Cell **156**, 183 (2014).
[5] D. Holcman, P. Parutto, J. E. Chambers, M. Fantham, L. J. Young, S. J. Marciniak, C. F. Kaminski, D. Ron, and E. Avezov, Single particle trajectories reveal active endoplasmic reticulum luminal flow, Nat Cell Biol **20**, 1118 (2018).
[6] M. Guo, A. J. Ehrlicher, M. H. Jensen, M. Renz, J. R. Moore, R. D. Goldman, J. Lippincott-Schwartz, F. C. Mackintosh, and D. A. Weitz, Probing the stochastic, motor-driven properties of the cytoplasm using force spectrum microscopy, Cell **158**, 822 (2014).
[7] N. Gal, D. Lechtman-Goldstein, and D. Weihs, Particle tracking in living cells: a review of the mean square displacement method and beyond, Rheol Acta **52**, 425 (2013).
[8] E. F. Koslover, C. K. Chan, and J. A. Theriot, Disentangling random motion and flow in a complex medium, Biophys J **110**, 700 (2016).
[9] C. Lin, M. Schuster, S. C. Guimaraes, P. Ashwin, M. Schrader, J. Metz, C. Hacker, S. J. Gurr, and G. Steinberg, Active diffusion and microtubule-based transport oppose myosin forces to position organelles in cells, Nature Comm **7**, 11814 (2016).
[10] K. Chen, B. Wang, and S. Granick, Memoryless self-reinforcing directionality in endosomal active transport within living cells, Nat Mater **14**, 589 (2015).
[11] Š. Bálint, I. V. Vilanova, Á. S. Álvarez, and M. Lakadamyali, Correlative live-cell and superresolution microscopy reveals cargo transport dynamics at microtubule intersections, P Natl Acad Sci **110**, 3375 (2013).
[12] D. Weihs, T. G. Mason, and M. A. Teitell, Biomicrorheology: a frontier in microrheology, Biophys J **91**, 4296 (2006).
[13] S. C. Weber, A. J. Spakowitz, and J. A. Theriot, Nonthermal ATP-dependent fluctuations contribute to the in vivo motion of chromosomal loci, P Natl Acad Sci **109**, 7338 (2012).
[14] É. Fodor, M. Guo, N. Gov, P. Visco, D. Weitz, and F. van Wijland, Activity-driven fluctuations in living cells, EPL (Europhysics Letters) **110**, 48005 (2015).
[15] P. Kollmannsberger and B. Fabry, Linear and nonlinear rheology of living cells, Annu Rev Mater Res **41**, 75 (2011).
[16] S. C. Weber, M. A. Thompson, W. E. Moerner, A. J. Spakowitz, and J. A. Theriot, Analytical tools to distinguish the effects of localization error, confinement, and medium elasticity on the velocity autocorrelation function, Biophys J **102**, 2443 (2012).
[17] R. Metzler and J. Klafter, The random walk's guide to anomalous diffusion: a fractional dynamics approach, Physics reports **339**, 1 (2000).
[18] Y. Wang, R. H. Austin, and E. C. Cox, Single molecule measurements of repressor protein 1d diffusion on DNA, Phys Rev Lett **97**, 048302 (2006).
[19] H. Li, S.-X. Dou, Y.-R. Liu, W. Li, P. Xie, W.-C. Wang, and P.-Y. Wang, Mapping intracellular diffusion distribution using single quantum dot tracking: compartmentalized diffusion defined by endoplasmic reticulum, J Am Chem Soc **137**, 436 (2015).
[20] F. Etoc, E. Balloul, C. Vicario, D. Normanno, D. Liße, A. Sittner, J. Piehler, M. Dahan, and M. Coppey, Non-specific interactions govern cytosolic diffusion of nanosized objects in mammalian cells, Nat Mater **17**, 740 (2018).
[21] S. Yamada, D. Wirtz, and S. C. Kuo, Mechanics of living cells measured by laser tracking microrheology, Biophys J **78**, 1736 (2000).
[22] B. D. Hoffman, G. Massiera, K. M. Van Citters, and J. C. Crocker, The consensus mechanics of cultured mammalian cells, P Natl Acad Sci **103**, 10259 (2006).
[23] A. Sabri, X. Xu, D. Krapf, and M. Weiss, Elucidating the origin of heterogeneous anomalous diffusion in the cytoplasm of mammalian cells, Phys Rev Lett **125**, 058101 (2020).
[24] J. S. Lucas, Y. Zhang, O. K. Dudko, and C. Murre, 3D trajectories adopted by coding and regulatory dna elements: first-passage times for genomic interactions, Cell **158**, 339 (2014).
[25] B. Wang, J. Kuo, S. C. Bae, and S. Granick, When brownian diffusion is not gaussian, Nat Mater **11**, 481 (2012).
[26] T. J. Lampo, S. Stylianidou, M. P. Backlund, P. A. Wiggins, and A. J. Spakowitz, Cytoplasmic RNA-protein particles exhibit non-gaussian subdiffusive behavior, Biophys J **112**, 532 (2017).
[27] S. S. Mogre, A. I. Brown, and E. F. Koslover, Getting around the cell: physical transport in the intracellular world, Phys Biol **17**, 061003 (2020).
[28] M. H. Duits, Y. Li, S. A. Vanapalli, and F. Mugele, Mapping of spatiotemporal heterogeneous particle dynamics in living cells, Phys Rev E **79**, 051910 (2009).
[29] A. V. Chechkin, F. Seno, R. Metzler, and I. M. Sokolov, Brownian yet non-gaussian diffusion: from superstatistics to subordination of diffusing diffusivities, Physical Review X **7**, 021002 (2017).
[30] J. Adler, I.-M. Sintorn, R. Strand, and I. Parmryd, Conventional analysis of movement on non-flat surfaces like the plasma membrane makes brownian motion appear anomalous, Communications biology **2**, 1 (2019).
[31] M. J. Saxton, Single-particle tracking: effects of corrals, Biophys J **69**, 389 (1995).
[32] M. P. Viana, A. I. Brown, I. A. Mueller, C. Goul, E. F. Koslover, and S. M. Rafelski, Mitochondrial Fission and Fusion Dynamics Generate Efficient, Robust, and Evenly Distributed Network Topologies in Budding Yeast Cells, Cell Syst **10**, 287 (2020).
[33] D. S. Schwarz and M. D. Blower, The endoplasmic reticulum: structure, function and response to cellular signaling, Cell Mol Life Sci **73**, 79 (2016).
[34] H. T. Perkins and V. Allan, Intertwined and finely balanced: Endoplasmic reticulum morphology, dynamics, function, and diseases, Cells **10**, 2341 (2021).
[35] L. Westrate, J. Lee, W. Prinz, and G. Voeltz, Form follows function: the importance of endoplasmic reticulum shape, Annu Rev Biochem **84**, 791 (2015).
[36] J. R. Friedman and G. K. Voeltz, The ER in 3D: a multifunctional dynamic membrane network, Trends Cell Biol **21**, 709 (2011).
[37] S. Chen, P. Novick, and S. Ferro-Novick, ER structure and function, Curr Opin Cell Biol **25**, 428 (2013).
[38] L. R. Griffing, Networking in the endoplasmic reticulum, Biochem Soc T **38**, 747 (2010).
[39] C. Barlowe and A. Helenius, Cargo capture and bulk flow in the early secretory pathway, Annu Rev Cell Dev Bi **32**,

197 (2016).
[40] A. I. Brown, L. M. Westrate, and E. F. Koslover, Impact of global structure on diffusive exploration of organelle networks, Sci Rep **10**, 1 (2020).
[41] Z. C. Scott, A. I. Brown, S. S. Mogre, L. M. Westrate, and E. F. Koslover, Diffusive search and trajectories on tubular networks: a propagator approach, Eur Phys J E **44**, 1 (2021).
[42] L. Stadler, K. Speckner, and M. Weiss, Diffusion of exit sites on the endoplasmic reticulum: a random walk on a shivering backbone, Biophys J **115**, 1552 (2018).
[43] M. Dora and D. Holcman, Active flow network generates molecular transport by packets: case of the endoplasmic reticulum, Proceedings of the Royal Society B **287**, 20200493 (2020).
[44] M. J. Dayel, E. F. Hom, and A. S. Verkman, Diffusion of green fluorescent protein in the aqueous-phase lumen of endoplasmic reticulum, Biophys J **76**, 2843 (1999).
[45] E. D. Siggia, J. Lippincott-Schwartz, and S. Bekiranov, Diffusion in inhomogeneous media: theory and simulations applied to whole cell photobleach recovery, Biophysical journal **79**, 1761 (2000).
[46] S. Nehls, E. L. Snapp, N. B. Cole, K. J. Zaal, A. K. Kenworthy, T. H. Roberts, J. Ellenberg, J. F. Presley, E. Siggia, and J. Lippincott-Schwartz, Dynamics and retention of misfolded proteins in native ER membranes, Nature cell biology **2**, 288 (2000).
[47] T. Konno, P. Parutto, D. M. Bailey, V. Davì, C. Crapart, M. A. Awadelkareem, C. Hockings, A. Brown, K. M. Xiang, A. Agrawal, *et al.*, Endoplasmic reticulum morphological regulation by rtn4/nogo modulates neuronal regeneration by slowing luminal transport, bioRxiv (2021).
[48] F. Santamaria, S. Wils, E. De Schutter, and G. J. Augustine, Anomalous diffusion in purkinje cell dendrites caused by spines, Neuron **52**, 635 (2006).
[49] F. Sartori, A.-S. Hafner, A. Karimi, A. Nold, Y. Fonkeu, E. M. Schuman, and T. Tchumatchenko, Statistical laws of protein motion in neuronal dendritic trees, Cell Rep **33**, 108391 (2020).
[50] W. Deng and E. Barkai, Ergodic properties of fractional brownian-langevin motion, Phys Rev E **79**, 011112 (2009).
[51] J.-H. Jeon and R. Metzler, Fractional brownian motion and motion governed by the fractional langevin equation in confined geometries, Phys Rev E **81**, 021103 (2010).
[52] S. M. Ross, *Introduction to probability models* (Academic press, 2014).
[53] Y. Dodge, *The concise encyclopedia of statistics* (Springer Science & Business Media, 2008).
[54] P. C. Bressloff and J. M. Newby, Stochastic models of intracellular transport, Rev Mod Phys **85**, 135 (2013).
[55] S. C. Weber, A. J. Spakowitz, and J. A. Theriot, Bacterial chromosomal loci move subdiffusively through a viscoelastic cytoplasm, Phys Rev Lett **104**, 238102 (2010).
[56] D. Kroese and Z. Botev, Spatial process simulation, in *Stochastic Geometry, Spatial Statistics, and Random Fields*, edited by V. Schmidt (Springer International Publishing, 2015) Chap. 12, pp. 369–403.
[57] S. C. Weber, J. A. Theriot, and A. J. Spakowitz, Subdiffusive motion of a polymer composed of subdiffusive monomers, Phys Rev E **82**, 011913 (2010).
[58] L. K. Schroeder, A. E. Barentine, H. Merta, S. Schweighofer, Y. Zhang, D. Baddeley, J. Bewersdorf, and S. Bahmanyar, Dynamic nanoscale morphology of the ER surveyed by STED microscopy, Journal of Cell Biology **218**, 83 (2019).
[59] D. P. Hoffman, G. Shtengel, C. S. Xu, K. R. Campbell, M. Freeman, L. Wang, D. E. Milkie, H. A. Pasolli, N. Iyer, J. A. Bogovic, *et al.*, Correlative three-dimensional super-resolution and block-face electron microscopy of whole vitreously frozen cells, Science **367**, eaaz5357 (2020).
[60] L. Heinrich, D. Bennett, D. Ackerman, W. Park, J. Bogovic, N. Eckstein, A. Petruncio, J. Clements, S. Pang, C. S. Xu, *et al.*, Whole-cell organelle segmentation in volume electron microscopy, Nature **599**, 141 (2021).
[61] J. R. Friedman, B. M. Webster, D. N. Mastronarde, K. J. Verhey, and G. K. Voeltz, ER sliding dynamics and er–mitochondrial contacts occur on acetylated microtubules, J Cell Biol **190**, 363 (2010).
[62] C. Lin, R. R. White, I. Sparkes, and P. Ashwin, Modeling endoplasmic reticulum network maintenance in a plant cell, Biophys J **113**, 214 (2017).
[63] C. Lee and L. B. Chen, Dynamic behavior of endoplasmic reticulum in living cells, Cell **54**, 37 (1988).
[64] C. Lee, M. Ferguson, and L. B. Chen, Construction of the endoplasmic reticulum., The Journal of cell biology **109**, 2045 (1989).
[65] M. Barthélemy, Spatial networks, Physics Reports **499**, 1 (2011).
[66] N. Malchus and M. Weiss, Anomalous diffusion reports on the interaction of misfolded proteins with the quality control machinery in the endoplasmic reticulum, Biophys J **99**, 1321 (2010).
[67] S. Wang, H. Tukachinsky, F. B. Romano, and T. A. Rapoport, Cooperation of the ER-shaping proteins atlastin, lunapark, and reticulons to generate a tubular membrane network, eLife **5**, e18605 (2016).
[68] MATLAB, *version 9.5 (R2018b)* (The MathWorks Inc., Natick, Massachusetts, 2018).
[69] G. J. Papadopoulos and J. T. Devreese, *Path Integrals: And Their Applications in Quantum, Statistical and Solid State Physics*, Vol. 34 (Springer Science & Business Media, 2013).
[70] P. Sengupta, T. Jovanovic-Talisman, and J. Lippincott-Schwartz, Quantifying spatial organization in point-localization superresolution images using pair correlation analysis, Nature protocols **8**, 345 (2013).
[71] L. M. Costantini, M. Baloban, M. L. Markwardt, M. A. Rizzo, F. Guo, V. V. Verkhusha, and E. L. Snapp, A palette of fluorescent proteins optimized for diverse cellular environments, Nature communications **6**, 1 (2015).
[72] G. V. Los, L. P. Encell, M. G. McDougall, D. D. Hartzell, N. Karassina, C. Zimprich, M. G. Wood, R. Learish, R. F. Ohana, M. Urh, *et al.*, Halotag: a novel protein labeling technology for cell imaging and protein analysis, ACS chemical biology **3**, 373 (2008).
[73] L. P. Encell, R. F. Ohana, K. Zimmerman, P. Otto, G. Vidugiris, M. G. Wood, G. V. Los, M. G. McDougall, C. Zimprich, N. Karassina, *et al.*, Suppl 1: Development of a dehalogenase-based protein fusion tag capable of rapid, selective and covalent attachment to customizable ligands, Current chemical genomics **6**, 55 (2012).
[74] J. Nixon-Abell, C. J. Obara, A. V. Weigel, D. Li, W. R. Legant, C. S. Xu, H. A. Pasolli, K. Harvey, H. F. Hess, E. Betzig, *et al.*, Increased spatiotemporal resolution reveals highly dynamic dense tubular matrices in the peripheral ER, Science **354** (2016).

[75] J. B. Grimm, B. P. English, H. Choi, A. K. Muthusamy, B. P. Mehl, P. Dong, T. A. Brown, J. Lippincott-Schwartz, Z. Liu, T. Lionnet, *et al.*, Bright photoactivatable fluorophores for single-molecule imaging, Nature methods **13**, 985 (2016).
[76] S. Berg, D. Kutra, T. Kroeger, C. N. Straehle, B. X. Kausler, C. Haubold, M. Schiegg, J. Ales, T. Beier, M. Rudy, K. Eren, J. I. Cervantes, B. Xu, F. Beuttenmueller, A. Wolny, C. Zhang, U. Koethe, F. A. Hamprecht, and A. Kreshuk, Ilastik: interactive machine learning for (bio)image analysis, Nat Methods 10.1038/s41592-019-0582-9 (2019).
[77] J.-Y. Tinevez, N. Perry, J. Schindelin, G. M. Hoopes, G. D. Reynolds, E. Laplantine, S. Y. Bednarek, S. L. Shorte, and K. W. Eliceiri, Trackmate: An open and extensible platform for single-particle tracking, Methods **115**, 80 (2017).
[78] K. Jaqaman, D. Loerke, M. Mettlen, H. Kuwata, S. Grinstein, S. L. Schmid, and G. Danuser, Robust single-particle tracking in live-cell time-lapse sequences, Nature methods **5**, 695 (2008).
[79] Y. Li, M. Mund, P. Hoess, J. Deschamps, U. Matti, B. Nijmeijer, V. J. Sabinina, J. Ellenberg, I. Schoen, and J. Ries, Real-time 3d single-molecule localization using experimental point spread functions, Nature methods **15**, 367 (2018).

Appendix A: Methods

All code used in this work was written in Matlab [68]. A software package for carrying out simulations on networks and for analyzing particle trajectories is provided at `https://github.com/lenafabr/unravelNetworkTraj`.

1. Algorithm for Brownian motion simulations on networks

We develop an algorithm for discrete time-step simulations of Brownian particles on a network of one-dimensional edges connected by point-like junctions, as discussed in Sec. II A.

At each step, for each individual particle, we consider the particle's position along its current edge. Without loss of generality, we can assume that the nearest boundary (node) of that edge is at position 0 and the particle itself is at position x_0 along the edge. We sample the net displacement of an unconstrained Brownian particle over time interval Δt from the Gaussian propagator function of such particles (namely, $\Delta z \sim \mathcal{N}(0, \sqrt{2D\Delta t})$). We note that this normally-distributed displacement over the time-interval incorporates an infinite number of particle paths, as in the classic path-integral formulation of Brownian motion [69]. We consider, of all possible paths that start at x_0 and end at $x_0 + \Delta z$, what is the probability that the particle's path crossed 0 during that timestep. This probability p_{pass} is derived as follows.

We start with the Green's function for unconstrained diffusion:

$$G(x|x_0, \Delta t) = \frac{1}{\sqrt{4\pi D\Delta t}} e^{-(x-x_0)^2/4D\Delta t}, \tag{A1}$$

which gives the spatial probability density of a particle ending its path at position x after time Δt, given that it started at position x_0 at time 0. The distribution of first passage times for a particle starting at x_0 to hit 0 for the first time at time t is given by

$$J(t; x_0) = D\, \frac{\partial}{\partial x} G(x|x_0; t)\bigg|_{x=0}. \tag{A2}$$

Because diffusion is Markovian (memory-less), if the particle first hits 0 at time t, we know the probability density of ending up at position x is simply given by $G(x|0, \Delta t - t)$. From there, we can calculate the conditional probability that a particle hit 0 at some point in the path, given that it ended at x, by a simple application of Bayes' rule:

$$p_{\text{pass}} = \frac{\int_0^{\Delta t} J(t; x_0) G(x|0, \Delta t - t) dt}{G(x|x_0, \Delta t)}. \tag{A3}$$

Here, the numerator is the joint probability density of hitting 0 at some point during the time-step and then ending the path at x and the denominator is the overall probability density of ending at x. Plugging in Eq. A1 and A2 gives the formula for p_{pass} stated in the main text (Eq. 1).

Every path of an unconstrained particle can be mapped to a set of 'folded' paths for the equivalent particle on the network. Each passage of the node at 0 involves selecting which of the adjacent network edges will serve as the axis along which the network-bound particle continues to move. For a memory-less Brownian particle that hits the node, each of the edges (including the one from whence it came) are equally likely to be selected. We know the unconstrained particle ends its timestep at distance $|x_0 + \Delta z|$ from 0. Hence, the network-confined particle is placed at this distance from the node along the randomly selected edge, completing its time-step.

2. Distribution of diffusing particles on a triskelion

We compute explicitly the solution to the diffusion equation on a triskelion structure (Fig. 1b) with reflecting boundaries at the tips and continuity of the concentrations at the degree-3 node. The initial condition is assumed to be a delta function at the junction. The approach taken is analogous to the equivalent problem with absorbing boundaries, described in more detail in Ref. [41]. Specifically, after a Laplace transform in time ($t \to s$), the concentration profile $\hat{c}_k(x, s)$ on edge k is given by

$$\hat{c}_k(x, s) = \frac{1}{D\alpha} \frac{\cosh \alpha x}{\cosh \alpha \ell_k} \left[\sum_{j=1}^{3} \tanh \alpha \ell_j \right]^{-1} \tag{A4}$$

where D is the particle diffusion coefficient, $\alpha = \sqrt{s/D}$, and ℓ_j is the length of the j^{th} edge.

The Laplace transform is then inverted using a Bromwich integral evaluated with the Cauchy residue theorem, yielding the time-dependent concentration profile

$$c(x,t) = \sum_p r_p e^{-Du_p^2 t}, \tag{A5}$$

where the poles $s_p = -Du_p^2$ can be found by taking the roots of the following equation:

$$\cos \ell_k u_p \left[\sum_j \tan \ell_j u_p \right] = 0, \tag{A6}$$

and r_p are the residues of Eq. A4 at those poles.

The resulting expressions are plotted in Fig. 1b and compared to the distribution of 10^7 simulated particles at time $t = 0.8\ell^2/D$ (after starting at the three-fold junction) where ℓ is the length of the shortest edge.

3. Parameters for simulations and analysis

a. Brownian motion on networks

The simulations are tested on synthetic networks, as well as network structures extracted from images of the ER. For comparing particle distributions on the triskelion network (Fig. 1b), 10^7 particles were simulated with timesteps of $\Delta t D/\ell^2 = 0.01$, for 80 steps. All particles were started on the central node.

The synthetic honeycomb network in Fig. 1c was created by cropping a standard honeycomb lattice with $N = 15$ cells in each dimension to a circle of radius 1. All reported length units for simulations on synthetic networks are normalized by the single edge length ℓ in the network. The diluted honeycomb structure was obtained by removing 30% of all network edges, randomly selected in such a way that the network maintains a single connected component. While all the example networks used in this study are two-dimensional, the simulations and unraveling code also applies to 3D networks.

Brownian simulations for the MSD comparison were run with 100 particles, using dimensionless timesteps of $\Delta t D/\ell^2 = 0.01$, for up to $N_t = 3 \times 10^4$ time steps. The mean squared dispacement (MSD) is computed as $\text{MSD} = \left\langle |\vec{x}(t) - \vec{x}(0)|^2 \right\rangle$, where the average is done over non-overlapping time-windows of a single trajectory and over all particle trajectories.

b. Trajectory unraveling analysis

The algorithm for unraveling observed trajectories on a network to sample the corresponding trajectories on an infinite line is described in Sec. II C. We perform the unraveling procedure with 20 values of diffusion coefficient in the range $0.2 - 2$ (compared to the simulated value of $D = 1$). Residuals are calculated by interpolating each unravelled MSD curve onto 100 logarithmically spaced time-points and then applying Eq. 9. The self-consistent diffusion coefficient is then found by estimating the value of D that yields a local minimum in the normalized residuals curve (eg: Fig. 2c) via a cubic spline interpolation.

4. Simulation of fractional Langevin motion on networks

The long-tailed memory kernel of fractional Langevin motion implies that individual steps of such particles are not Markovian, necessitating an alternate approach to the simulation. We take the approach of assuming that individual particles are undergoing fLM in two dimensions, but that rapid reflections from the walls of a narrow tubule prevent their perpendicular motion and force them to always land on the tubule axis. Our overall approach is analogous to that described previously [51] for simulating the fractional Langevin equation under confinement, in the limit of no inertia (as appropriate for highly viscous intracellular fluids). The particles maintain a memory of their past displacements in the 2D imaging plane as they move throughout the network.

Specifically, we consider the power-law memory kernel [57]

$$K(t-t') = \frac{(2-\alpha)(1-\alpha)}{|t-t'|^\alpha} \tag{A7}$$

and generate 2D stochastic forces $F_x^{(B)}, F_y^{(B)}$ as fractional Gaussian noise [56] with time correlations in accordance with the fluctuation dissipation theorem:

$$\left\langle F_i^{(B)}(t) F_j^{(B)}(t') \right\rangle = \gamma k_b T K(t-t') \delta_{ij},$$

where γ is the friction coefficient and $k_b T$ the thermal energy of the particles. We note that this approach is also applicable in 3D, although we have focused on planar networks here to match the two-dimensional trajectories extracted from experimental data.

The particle motion obeys the overdamped Langevin equation:

$$0 = -\gamma \int_0^t K(t-t')\vec{v}(t')dt' + \vec{F}^{(b)}(t) \tag{A8}$$

where $\vec{v}(t')$ is the instantaneous particle velocity. In the absence of confinement, the MSD for such particles is described by the following power law [57]:

$$\begin{aligned} \left\langle x^2 \right\rangle &= 2D_\alpha t^\alpha, \\ D_\alpha &= \frac{k_b T/\gamma}{(2-\alpha)(1-\alpha)\Gamma(\alpha+1)\Gamma(1-\alpha)}. \end{aligned} \tag{A9}$$

To propagate forward the particles via discrete timesteps, we take the approach described in Ref. [50]. Namely, we discretize the integral in Eq. A8 and solve for the next trial spatial step $\Delta\widehat{\vec{x}}_{n+1}$ based on all prior steps $\Delta\vec{x}_{n+1}$ and the fractional Brownian force $\vec{F}^{(B)}_{n+1}$.

The trial step $\Delta\widehat{\vec{x}}$ is then projected along the direction of the current edge containing the particle (removing the perpendicular component). If the remaining step takes the particle past a degree-1 node (dead end), it is reflected off the node, back along the same edge. If it steps past a degree-3 node, then it is placed randomly on one of the adjacent edges (including the one it came from). For our simulated networks, edges are evenly distributed around each such junction, so that multiple reflections in the tight junctional space are expected to be equally likely to bounce the particle to any edge. Application of this algorithm to more complex structures, including bent degree-2 nodes and degree-3 nodes with uneven edge distribution would require further refinement of this algorithm (left to future work) to account for biased probabilities of entering subsequent edges.

The final saved step $\Delta\vec{x}$ is then computed as the two-dimensional difference between the final particle position and its prior position at the start of the step. This saved step is used in the computation of all future particle displacements, allowing the particle to maintain a memory of its prior speed and direction of motion.

We note that this simulation approach gives the expected mean squared displacement of $2D_\alpha t^\alpha$ when particles are placed along a single long edge or along a fully connected honeycomb lattice (Supplemental Fig. S3).

5. Experimental methods

a. Cell culture, plating, and transfection

COS7 cells were purchased from ATCC and maintained in phenol red-free Dulbeccos modified Eagle medium supplemented with 10% (v/v) FBS, 2mM L-glutamine, 100U/ml penicillin and 100μg/ml streptomycin at 37°C and 5% CO_2. All experiments were performed within 40 passages of the initial thaw, and passaging was performed using phenol red-free trypsin (Corning).

High tolerance, 25mm Number 1.5 coverslips were purchased from Warner scientific and precleaned with a modified version of a previously described protocol [70]. Briefly, the coverslips were sonicated for 12 hours in 0.1% Hellmenex (Sigma), followed by five washes in 300ml of distilled water, followed by an additional 12 hour sonication in distilled water and an additional round of five washes. Coverslips were then ethanol sterilized in 200 proof ethanol and allowed to air dry in a clean tissue culture hood. After cleaning, coverslips were stored in an airtight container until ready for use.

Coverslips were pre-coated with 500μg/ml phenol red-free matrigel (Corning). Cells were seeded to achieve 60% confluency at the time of imaging. Transfections were performed after letting the cells adhere to the coated glass for at least 12 hours, using Fugene6 (Promega) according to the manufacturer's protocol. Each coverslip was transfected with 750 ng of PrSS-mEmerald-KDEL to label the ER structure in the 488nm channel, and with 250ng of HaloTag-Sec61b-TA for tracking on the second camera. PrSS-mEmerald-KDEL uses the signal sequence of bovine prolactin to target the fluorescent protein mEmerald to the ER lumen, where it is retained through the use of a KDEL retention signal at the C-terminus, as performed in [71]. The HaloTag construct is a minimal targeting domain from Sec61b fused with a flexible linker and the HaloTag [72, 73], as this construct has been shown to be biochemically inert within the ER[74].

b. Labeling conditions

Immediately before imaging, each sample was labeled with 10nM PA-JF646 [75] in OptiMEM (ThermoFisher) for 1 minute. PA-JF646 is a diazoketone-caged version of the azetidine-containing Si-rhodamine JF-646, which shows high signal to noise and low background at the single molecule level when uncaged with 405 nm light [75]. Following staining, cells were immediately washed at least 5 times with 10 ml of PBS under continuous aspiration, taking care not to let the cells contact the air. This was followed by an additional wash in 10 ml of pre-warmed, complete medium. Samples were then left 10 minutes in an incubator to let the cells recover before moving immediately to the microscope.

c. Microscope and imaging conditions

Dual-color imaging was performed using a customized inverted Nikon Ti-E microscope outfitted with a live imaging stage to maintain temperature, CO_2 level, and relative humidity during imaging (Tokai Hit). The sample was illuminated with two fiber-coupled 488nm and 642nm lasers (Agilent Technologies) introduced into the system with a conventional rear-mount TIRF illuminator. Imaging was performed with the angle of incidence of excitation light manually adjusted beneath the critical angle as needed to produce the most even illumination possible in the ER. If necessary, a small amount of 405nm light was introduced to increase the rate of photoconversion in sparsely labeled cells, but in practice this was rarely needed. The 488 illumination power was kept beneath 100 μW total in the back aperture, in order to avoid undesirable activation of the photoconvertible dye.

Fluorescence emission light was collected with 100x α-Plan-Apochromat 1.49 NA oil objective (Nikon Instruments). Emission light was split into dual paths using a 565LP or 585LP dichroic mirror in a MultiCam

optical splitter (Cairn Research), and the two channels were cleaned up by passing the light through 525/50 and 647LP filters (Chroma) placed before the camera. Final signal was focused back onto synchronized dual iXon3 electron mutliplying charged coupled device cameras (EM-CCD, DU-897; Andor Technology). In this set up, the raw image has pixels of 160nm × 160nm, and the depth of focus has a full width half maximum of approximately 700nm. Total image size was limited to 128x128 pixels (20.48μm x 20.48μm) in order to keep camera readout time from becoming rate limiting. Imaging was performed with 5ms exposure times for 60-90 seconds at a time, and the timing of each frame was monitored using an oscilloscope directly coupled into the system (mean frame rate $\approx$ 95Hz).

6. Image analysis for experimental data

a. *Image preparation and preprocessing*

The ER is relatively stable at the level of diffraction-limited imaging over the time scale of a second [61]. Thus, we performed 10 frame (110 msec) median filter on the channel for the ER structure to increase the signal to noise and minimize the necessary 488 radiation. Filtering was performed for every frame, but for segmentation and downstream analysis, the structure was analyzed approximately every second (100 frames).

b. *Segmentation*

Segmentation and analysis of the tubular ER structure was performed using a two-step process. First, the intensity in the filtered image was made uniform through time with a simple ratio bleach correction. The location of the ER within the image was identified using an interactive pixel classification workflow in Ilastik [76]. Once the predictions for the ER label were judged to be of sufficiently good quality, the image was made binary using a simple threshold on the label probability exported from ilastik.

c. *Extracting network structure*

For each binary segmented image of the ER structure, we skeletonize using the bwmorph subroutine in MATLAB, which also identifies junction pixels. Neighboring junction pixels are grouped into a single node located at their center of mass. We then use the bwtraceboundary subroutine to trace out the skeletonized edges starting from each node, until a neighboring node is reached. This is repeated until the full skeleton has been categorized into nodes and edges connecting specific node pairs. The path of the edge between each pair of connected node is smoothed using cubic splines. Network construction and manipulations is carried out using Matlab code provided at: `https://github.com/lenafabr/networktools`.

d. *Particle trajectories*

Single molecule localization and tracking was performed using the TrackMate plugin in Fiji [77, 78]. Single molecules visible in each frame are quality filtered such that the mean localization precision of retained molecules is in the range of 25nm, as estimated using the Cramér-Rao lower bound of an MLE fit [79]. Linking parameters were experimentally selected for each data set to minimize visible linkage artifacts as determined by eye. Datasets were then projected onto the simultaneously collected structure of the ER and manually curated to remove trajectory linkages that were close in 2D but far from one another in the underlying organelle.

In Supplemental Fig. S6, we show (using simulated trajectories) that localization errors below $\sim$ 50nm are not expected to significantly alter our estimates of the diffusion coefficient.

For each network structure, obtained at $\approx$ 1.08 sec (100 frame) intervals, we identify particle trajectory segments that fall within $\pm$100 frames of the timepoint corresponding to that structure. Those trajectories are then projected onto the network structure by finding the nearest point along the edge paths to each particle position. Because the time intervals surrounding each network structure overlap with each other, each trajectory segment enters the analysis twice by projection onto the structure before and after its time-point.

Whenever the original particle position is more than 2px ($\sim 0.3\mu$m) away from the nearest network edge, the projected point is removed and the trajectory is broken into separate segments. The trajectories are also broken whenever a particle appears to step onto a non-adjacent edge (bypassing more than one node) within a single time-step. Furthermore, trajectories are truncated when a particle disappears in a given frame, including instances where the particle steps outside of the field of view.

The projection step allows us to re-express a particle trajectory in terms of the edge index and position along the edge contour at each time step. Projected trajectories of length at least 10 time-steps were kept for analysis and unravelled using the same algorithm as for simulated data. An average of 380 projected trajectories per cell, with average length 48 timesteps (0.51 sec) were analyzed.

We note that the structure of ER tubule junctions is not well established, and it is possible that the tubule intersections are substantially larger than the point-like junctions considered in our model, or that particles could be preferentially trapped at junctions. However, by examining the distribution of projected particle trajectories (Supplemental Material, Figure S5), we see no evidence

of junction trapping or unusually large junction regions for the HaloTag-Sec61b-TA proteins tracked in our study, both of which would result in preferential localization near the network nodes.